Measuring Membrane Permeation Rates through the Optical Visualisation of a Single Pore

Sotiria Tsochataridou,[a‡] Greg A. Mutch,[a‡] Dragos Neagu,[a] Evangelos I. Papaioannou,[a] María Luisa Sanjuán,[b] Brian Ray,[a] Rosa I. Merino,[b] Víctor M. Orera,[b] and Ian S. Metcalfe[a]*

[a] Materials, Concepts and Reaction Engineering (MatCoRE) Research Group, School of Engineering, Newcastle University, Newcastle-upon-Tyne, NE1 7RU, UK

[b] Instituto de Ciencia de Materiales de Aragón, CSIC-Universidad de Zaragoza, C/ Pedro Cerbuna 12, 50009 Zaragoza, Spain

KEYWORDS. Gas separation; image analysis; kinetics; membranes; thermodynamics

ABSTRACT. Membranes are a critical technology for energy-efficient separation processes. The routine method of evaluating membrane performance is a permeation measurement. However, such measurements can be limited in terms of their utility: membrane microstructure is often poorly characterised, membranes or sealants leak, and conditions in the gas phase are poorly controlled and frequently far-removed from the conditions employed in the majority of real processes. Here we demonstrate a new integrated approach to determine permeation rates, using two novel supported molten-salt membrane geometries. In both cases, the membranes comprise a solid support with laser-drilled pores, which are infiltrated with a highly-CO_2 selective molten carbonate salt. First, we fabricate an optically-transparent single crystal, single-pore model

membrane by local laser drilling. By infiltrating the single pore with molten carbonate, monitoring the gas-liquid interface optically and using image analysis on gas bubbles within the molten carbonate (as they change volume upon controlled changes in gas composition) we extract CO_2 permeation rates with exceptional speed and precision. Additionally, in this arrangement, microstructural characterisation is more straightforward, and a sealant is not required, eliminating a major source of leakage. Furthermore, we demonstrate that the technique can be used to probe a previously unexplored driving force region, too low to access with conventional methods. Subsequently, we fabricate a leak-free tubular supported molten-salt membrane with 1000 laser-drilled pores (infiltrated with molten carbonate) and employ a CO_2-containing sweep gas in order to obtain permeation rates in a system that can be described with unprecedented precision. Together, the two approaches provide new ways to measure permeation rates with increased speed and at previously inaccesible conditions.

INTRODUCTION.

Membranes offer cost-effective and energy-efficient chemical separation, as compared to distillation, absorption and adsorption processes. As such, there is significant interest in developing membranes for use in CO_2 capture, where both the cost of, and CO_2 emissions resulting from the separation process must be low.[1–3] Gas separation membranes can operate by selectively removing components from a feed gas mixture, injecting them into a sweep gas, resulting in a permeate stream. Laboratory-scale permeation experiments often employ membranes with a small membrane area (~cm^2) and can use an inert gas as a sweep gas to generate the partial pressure driving force required for permeation (Fig. 1). Although such approaches do allow the measurement of a wide range of gases in single and multicomponent mixtures over a large

condition range, there are major drawbacks associated with this approach. Firstly, the use of an inert gas may result in an undefined driving force at the sweep gas inlet or at the very least a driving force which is linked to the permeation rate itself. One reason routine experiments resort to the use of an inert sweep gas, instead of a sweep gas containing a known amount of permeant, is that it can be challenging to measure a permeation signal superimposed on a large background already present on both sides of the membrane. This presents a challenge due to sensitivity limitations of routine gas analysis apparatus. Secondly, laboratory membranes are typically operated with a low stage-cut (the fraction of the permeant removed from the feed), which means the average driving force is large in comparison to membranes in application. An additional issue involves transmembrane leaks, which are often simply subtracted from the permeation signal to obtain the "true" permeation signal (in Fig. 1c N_2 is used as a leak detector). Overall, uncertainty in making accurate permeation measurements necessary for mechanistic understanding and scale-up is apparent in routine membrane experiments, and a large amount of membrane experimental data is irrelevant to practical operation.

Here we show how adopting a visual approach allows one to measure permeation in supported-liquid membranes in an entirely new way (Fig. 1). We translated the supported molten-salt membrane concept (where molten carbonate is employed as a CO_2-selective phase in an *e.g.* oxygen-ion conducting ceramic support),[4] to an optically transparent single-pore single crystal model membrane. The typical ceramic support with random pore architecture (Fig. 1a – c), was replaced by a single-crystal support, with a single pore laser-drilled into it (Fig. 1d). After the single pore had been infiltrated with molten carbonate, the growth and shrinkage of occluded gas bubbles inside the single pore was monitored visually during a change in the CO_2 mole fraction of the model membrane external environment (Fig. 1e). An example of bubble growth is available to

view at https://figshare.com/s/e3fdd9267c250e4b8934 with all experimental videos given as Supporting Information, Videos S1 – S6. In this arrangement, a dynamic equivalent of a routine membrane permeation experiment was produced where driving force conditions were accessed in discrete elements of time (in contrast to spatial variation in a normal membrane). The approach was validated by comparing bubble growth or shrinkage to the expected change in bubble volume based upon thermodynamic limits and permeation rates were extracted with a temporal resolution dependent only on the optical discretisation of the visual data. Carbon dioxide fluxes at driving forces inaccessible in routine permeation experiments were determined with high precision due to the well-defined membrane surface area produced by microfabrication. Overall, a new approach to measure permeation that can be extended to any supported-liquid membrane, for any gas separation is demonstrated.

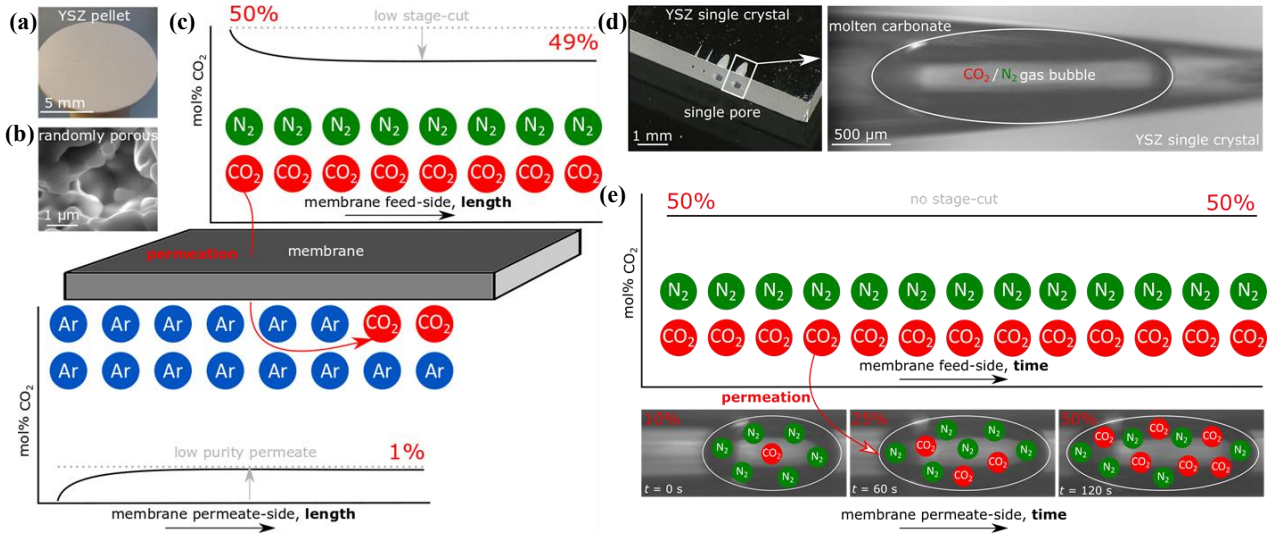

Figure. 1 Routine and visual permeation experiments. (a) Routine permeation measurements employ small pellet membranes (~cm^2) with a, **(b)** randomly porous microstructure. **(c)** Such a membrane is operated with a low stage-cut and often an inert sweep gas (Ar) which imposes a large average driving force along the length of the membrane. Furthermore, the use of an inert sweep gas implies an infinite driving force at the sweep-gas inlet, and a low-purity permeate gas. Such conditions are not found in application. **(d)** Employing a single-crystal model membrane with a laser-drilled single pore allows the visualisation of an effect of permeation. Here, a CO_2/N_2 bubble occluded by molten carbonate inside the single pore is exposed to a flowing gas with a higher mole fraction of CO_2. **(e)** Therefore, bubble volume increases with time and discrete driving forces can be accessed temporally. Note that during bubble growth, the permeate side of this

dynamic membrane is the bubble, and that there is CO_2 on both "sides" of the membrane at all times, addressing a fundamental limitation of routine permeation experiments.

RESULTS AND DISCUSSION.

Fabrication of single-crystal single-pore model membranes.

To facilitate the visualisation approach, a YSZ single crystal was laser drilled to form closed-end single pores of ~550 μm length and with ~100 μm Ø pore mouths (Supporting Information, Fig. S1). The laser drilled single pores were infiltrated with molten carbonate by placing a dried ternary eutectic carbonate mixture (Li/Na/K) at the pore mouth. The single crystal model membrane was then located inside an *in-situ* microscopic stage, coupled to mass flow regulated gas supplies and a temperature controller (Supporting Information, Fig. S2). A 50 ml min^{-1} (NTP) flow of a CO_2 in N_2 mixture was initiated, and during heating to 550 °C the carbonate mixture melted ($T_m \approx 400$ °C). Gas bubbles were routinely occluded by the infiltrating molten carbonate which was drawn into the pore by capillary forces (*i.e.* the CO_2 in N_2 mixture used during heating was trapped within the pore behind the infiltrating molten carbonate, typically resulting in the formation of a gas bubble). By manipulating the CO_2 mole fraction in the external environment of the single crystal model membrane (*i.e.* switching the flowing gas to one containing either a higher or lower mole fraction of CO_2), the bubble(s) would equilibrate with the external environment and increase or decrease in volume, respectively. The volume variation of the bubble was first determined using a simple manual image measurement of the entire bubble area, and then computationally using a proprietary code developed to distinguish pixel contrast and track representative points within the bubble. A full description of the methodology, including assumptions and calculations is provided in the Supporting Information.

Bubble growth and shrinkage measurements.

Growth and shrinkage of bubbles within the single-pore model membrane (Fig. 2a and b), extracted from videos during switches between 10 and 50 mol% CO_2 are shown as bubble volume normalised to the initial bubble volume from both manual and computational methods (Fig. 2c). The computational method provided high temporal resolution (0.255 s) with little effort compared to the manual method. Furthermore, data from both approaches agreed well, confirming that the tracked points were indeed representative of the overall bubble shape, indicating that the computational method provided robust data (Fig. 2c and Supporting Information, Fig. S3). Error in the determination of bubble volume using the computational method was ~±1% by comparing simple manual measurements to the computational approach, and from repeats. The most significant volume change occurred within the first ~30 s of a change in external gas phase composition, after which the rate of change decreased. As CO_2 permeates to equilibrate the internal and external gas compositions the difference between internal and external gas compositions is reduced, and thus the driving force for CO_2 permeation is also reduced. Generally, experiments were left to run for ~1 hour, however the majority of the expected volume change occurred within the first ~120 s, evidenced by the approach to the thermodynamic limits on bubble volume imposed by the respective change in CO_2 mole fraction (Fig. 2c).

Extraction of permeation rates from bubble volume changes.

Internal CO_2 mole fraction (*i.e.* inside the bubble) was then calculated from relative bubble volume changes, assuming the bubble pressure was close to atmospheric pressure, and that the pressure did not change significantly during growth or shrinkage (the total pressure can be expected to be within ~10% of atmospheric pressure (Supporting Information, Eq S1 – S3). Furthermore, it was assumed that permeation was selective to CO_2, reasonable considering the near perfect selectivity of molten carbonate membranes for CO_2 over N_2 (> 1000).[5] The high selectivity for CO_2 was

confirmed by comparison of observed bubble volume changes with those expected based upon thermodynamic considerations (Supporting Information, Eq S4 – S7). By considering the change of bubble CO_2 mole fraction in a discrete time element during the experiments, permeation rates were extracted (Supporting Information, Eq. S8). A sensitivity analysis for ± 1 and 20% errors on volume determination was shown to have negligible impact on the permeation rate determined, as the relative range in permeation rate did not change significantly (Supporting Information, Fig. S5). Within ~30 s, the visualisation approach accessed permeation rates over two orders of magnitude (shown as permeation rate normalised to the initial permeation rate in Fig. 2d and additional experiment, employing gas composition changes between 1.1 and 50 mol% CO_2 in Supporting Information Fig. S6). This represents a significant reduction in experimental time compared to routine membrane experiments which can take several hours to measure a stable permeation rate at one driving force.

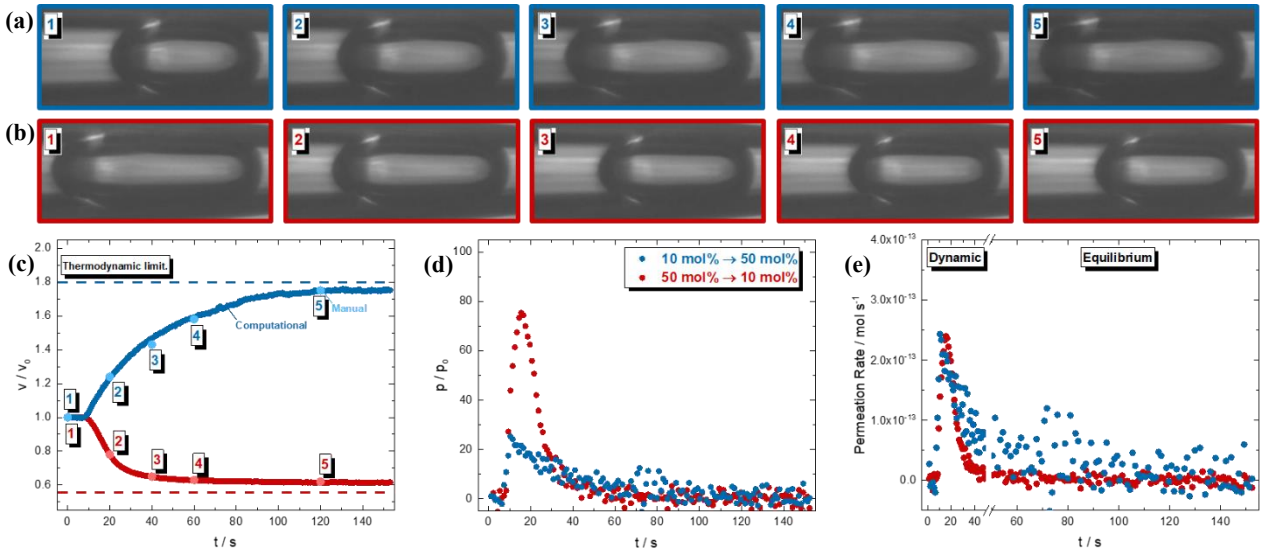

Figure. 2 Extraction of permeation rates from bubble volume changes. (a) Images of the growth of a 10 mol% CO_2 gas bubble following exposure to a flowing gas containing 50 mol% CO_2 and, **(b)** the reverse. **(c)** Normalised bubble volume variation calculated using manual image measurements at t = 0, 20, 40, 60 and 120 s (number labels correspond to images in (a) and (b)), and computational measurement of bubble volume with a temporal resolution of 0.255 s shown as a darker shade. The thermodynamic limit for bubble volume is shown as a dashed line (Supporting Information, Eq. S4 – S7). Detail on the manual and computational measurements is given in

Supporting Information, Fig. S3. **(d)** Normalised permeation rate variation extracted from experiments in (a) and (b) using Supporting Information, Eq. S8. **(e)** Absolute CO_2 permeation rates extracted from growth (a) and shrinkage (b) of CO_2/N_2 bubbles. During the initial ~30 s, the permeation rate increases then decreases (dynamic), as equilibrium with the external environment is approached. Subsequently (~60 – 150s), permeation rate remains low as the driving force for permeation is low (equilibrium). An additional experiment employing gas composition changes between 1.1 and 50 mol% CO_2 is given in Supporting Information, Fig. S6.

As the most significant volume change occurred within the first ~30 s (Fig. 2c), from an equilibrated starting point, it was expected that the permeation rate would increase to a maximum before decreasing as re-equilibration was approached. During this dynamic region of the experiment, calculated permeation rates ranged between 10^{-15} and 10^{-13} mol s^{-1} (Fig. 2e). Beyond ~30 s, bubble volume changes became far smaller, as equilibration with the new external environment approached completion (hence we refer to this as the equilibrium region). The scatter in the extracted permeation rates also increased in the equilibrium region as the bubble volume changes were now far smaller. However, a linear fitting of data points in *e.g.* Fig. 2e and Supporting Information, Fig S6 confirmed there was a small but measurable decrease in volume occurring during this period.

Flux determination at low driving forces.

This measurable decrease in permeation rate during the equilibrium region indicated that the visualisation approach could determine a CO_2 flux at low driving forces (*i.e.* when the CO_2 mole fraction of the bubble and external environment are very close). Determining CO_2 flux at low driving forces may be more appropriate for industrial membrane applications than the high driving forces typically adopted in the literature (Fig. 1). In industrial application, membranes will operate with a high stage-cut (a relevant example being CO_2 capture, where >90% capture is often required). Thus, driving forces in general are far lower than those tested in the laboratory (*i.e.* with significant mole fractions of CO_2 on both sides of the membrane).

Here, we first compiled data from routine supported molten-salt membrane experiments which employed a range of driving forces, oxygen-ion conducting support materials and membrane geometries in the supported molten-salt membrane literature (Fig. 3 and Supporting Information, Table S1).[6–14] CO_2 permeation in this class of membrane is commonly described as relying on ambipolar transport of CO_3^{2-} and O^{2-} ions in the melt and support respectively.[15] The anticipated CO_2 flux depends on a simple model that accounts for ionic conductivity and a logarithmic ratio of pCO_2 across the membrane (*i.e.* ln ($pCO_{2\ (feed)}/pCO_{2\ (permeate)}$)).[4,11,12,15,16] Next, the single-pore model membrane concept was extended to produce multiple-pore membranes, fabricated using the laser-drilling approach. Closed-end YSZ tubes were laser-drilled with 1000 single pores in the ~500 μm thick closed end (Supporting Information), and infiltrated with molten carbonate to form a supported molten-salt membrane (Fig. 4). A range of driving forces were probed using the multiple-pore membrane by supplying 90, 77, 50 and 25 mol% CO_2 as feed gases, and 1.1 mol% CO_2 or Ar as a sweep gas. Doing so, in certain cases, required the use of analytical apparatus at its limit of resolution (Supporting Information); for example, with the above feed gases the permeation signal superimposed on top of a 1.1 mol% CO_2 sweep gas, is routinely < 0.0025 mol% CO_2. However, it is important to note, that in these experiments we have precise control of the feed and sweep gas composition, unlike a routine permeation experiment where the sweep gas composition is a poorly-defined variable essentially determined by the CO_2 permeation rate. Single-pore permeation rates from growth and shrinkage experiments between 50 mol% CO_2 in N_2 and mixtures containing 10, 1.1 and 0.04 mol% CO_2 were converted to flux by dividing the permeation rate by the surface area of the single-pore mouth, assumed to be the surface area available for sorption and desorption of CO_2. For each experiment, an average permeation rate for 100 – 150s was extracted, and an average driving force (ln ($pCO_{2\ (feed)}/pCO_{2\ (permeate)}$)) for the same

time interval was calculated (Supporting Information Fig. S7). It is important to note that in Fig. 3, we show the data that was most challenging to extract, *i.e.* CO_2 fluxes from the lowest driving forces achieved. The technique can extract higher driving force fluxes, from the dynamic region.

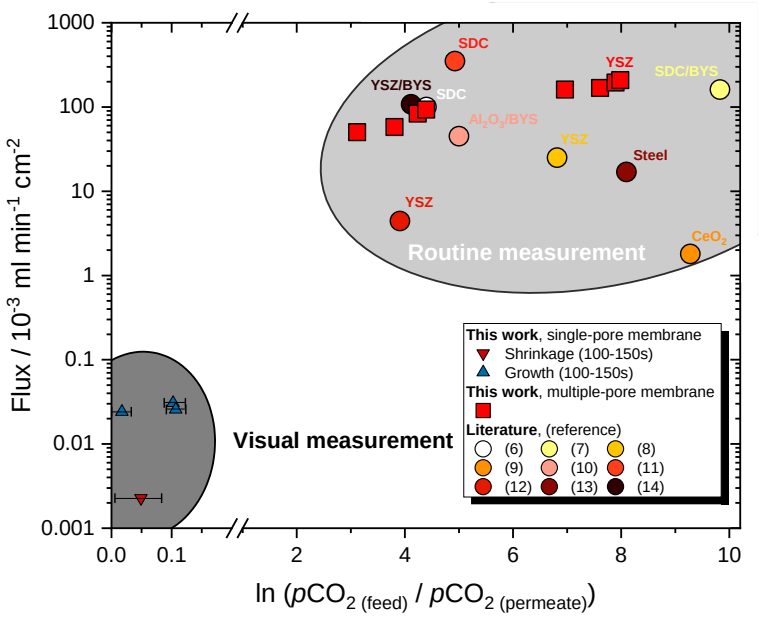

Figure. 3 Visual and routine flux measurements. Single-pore membranes and the visual method can probe a driving force region too challenging to access using routine measurements. Here, fluxes have been extracted from average permeation rates measured during 100 – 150 s in visual experiments (triangles and error bars, Supporting Information). The multiple-pore membrane accesses the routine measurement area but with a more well-defined membrane geometry. Representative data from the supported molten-salt membrane literature is provided (circles, with oxygen-ion conducting support material given). References in brackets can be referred to below.

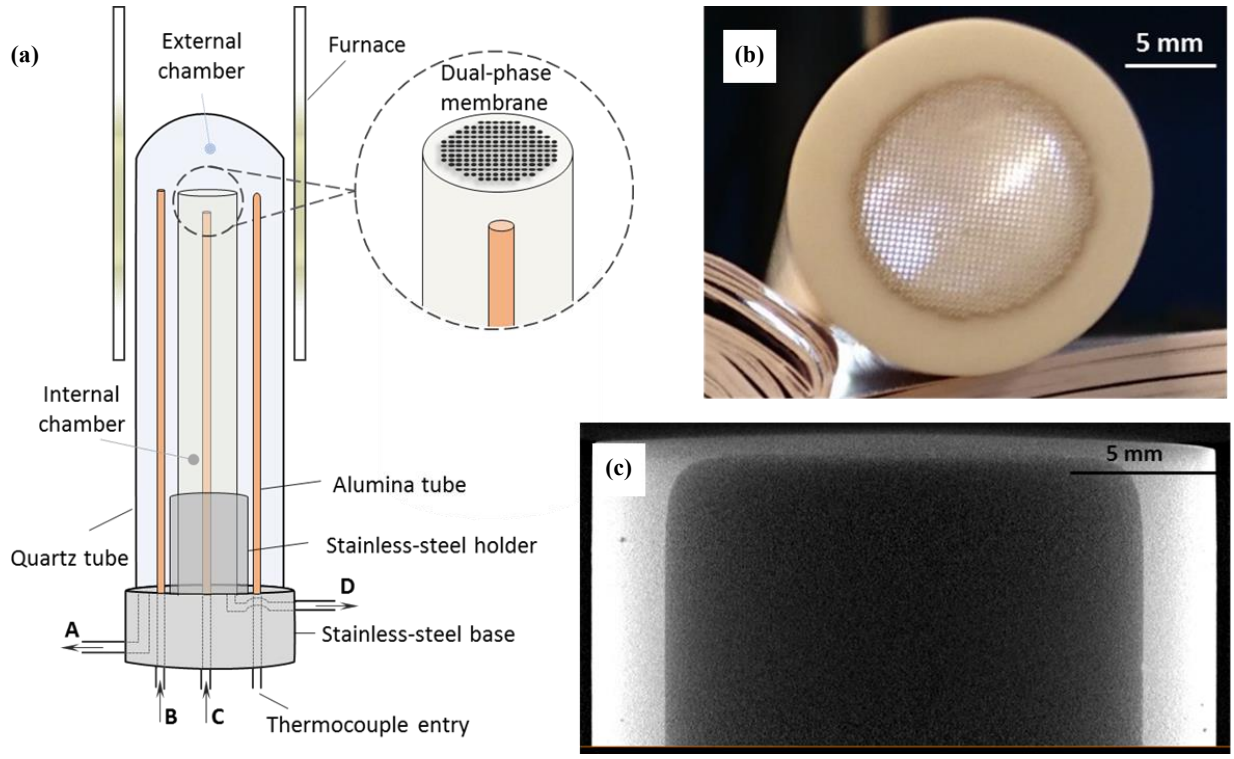

Figure. 4 Multiple-pore closed-end tube membrane and membrane reactor. (a) Multiple-pore membrane reactor, where A is the outlet of the feed-side chamber, with B the inlet, C is the inlet of the permeate-side chamber, with D the outlet. A thermocouple was positioned close to the membrane surface and the entire reactor placed within a furnace so that the stainless-steel base was outside the heating zone and a cold sealant could be used. **(b)** Digital image of the laser-drilled multiple-pore membrane. **(c)** X-ray micro-CT cross-section of the as-received closed-end tube.

CONCLUSIONS.

In summary, the multiple-pore membrane exposed the limitation of routine supported molten-salt permeation measurements, which have been limited to relatively high driving forces. However, by employing CO_2-containing sweep gases and pushing the limitations of routine analytical apparatus, the driving force region was modestly extended to lower driving forces (Fig 3). Moreover, the single-pore model membrane pushed flux measurement into an entirely unexplored driving force region and determined fluxes up to three orders of magnitude lower than has previously been possible in the relevant membrane literature. It is also important to note that both

the single- and multiple-pore membranes can be considered essentially leak-free; in the single-pore membrane this is due to the lack of requirement for a sealant, and in the case of the multiple-pore membrane, a new cold sealing procedure was developed which limited N_2 leakage to below the limit of detection of our analytical apparatus (~10 ppm) (Supporting Information). Thus, in both membrane geometries a fundamental limitation of routine supported molten-salt membrane experiments has been tackled; sealant failure and leakage. Furthermore, with well-defined structures and surface areas for sorption and desorption of CO_2 as a result of laser drilling, single- and multiple-pore membranes allow improved robustness in flux determination and use of a wide range of driving forces including access to a new low driving force region. The visualisation approach has been validated against simple thermodynamic expectations and is applicable to any supported-liquid membrane. Therefore, we believe the visualisation approach can be extended to a wide range of liquid-mediated gas separations (both supported-liquid membranes and absorption-based separations) and across length and time scales, with the following caveats. First, a microscopy technique capable of probing the required length and time scales is required. Second, the liquid should be suitably wetting on the optically-transparent material employed for the single-pore model membrane, so as to facilitate infiltration of the pore. Finally, consideration should be given to residence time distributions and relative time constants (mixing time versus characteristic permeation time). Overall, we have addressed a critical issue in membrane science – the need for new permeation measurement techniques,[17,18] applicable in complex environments at multiple scales.[19]

ASSOCIATED CONTENT

Supporting Information. Fabrication of single-crystal single-pore model membranes (Fig. S1); Visualisation experiment procedure (Fig. S2); Bubble growth and shrinkage measurements (Fig.

S3); Extraction of permeation rates from bubble volume changes and flux determination at low driving forces (Fig. S4 and S5); Supplemental permeation rate extraction from bubble volume changes (Fig. S6); Multiple-pore membrane preparation; Multiple-pore membrane experiment procedure; Literature data for flux comparison with single-pore and multiple-pore membranes (Table S1); Residence time distribution experiment for single-pore model membrane *in-situ* cell (Fig. S7).

The following files are available free of charge.

Videos S1 – S6: 0.04% to 50% (.avi); 1.1% to 50% (.avi); 10% to 50% (.avi); 50% to 0.04% (.avi); 50% to 1.1% (.avi); 50% to 10% (.avi).

AUTHOR INFORMATION

Corresponding Author

*Email: ian.metcalfe@newcastle.ac.uk

Author Contributions

‡These authors contributed equally.

ACKNOWLEDGMENT

Dedicated to the memory of Prof. Víctor M. Orera. The authors are grateful to Prof. Omar K. Matar for helpful discussions, Dr Thomas Miller for conducting the X-ray micro-CT, and the contribution of Dr Daniel Sola to the preparation of single-crystal supports in the early stage of this work. The research leading to these results has received funding from the European Research Council under the European Union's Seventh Framework Programme (FP/2007-2013) / ERC Grant Agreement Number 320725 and from the Engineering & Physical Sciences Research Council (EPSRC) *via*

grants EP/M01486X/1, EP/P007767/1 and EP/P009050/1. G.A.M. would like to thank the EPSRC for his Doctoral Prize Fellowship (EP/M50791X/1) and Newcastle University for a Newcastle University Academic Track (NUAcT) Fellowship. Financial support from the Spanish Ministerio de Economía y Competitividad and Feder Funds under project MAT2016-77769-R is acknowledged. Data supporting this publication is available under a Creative Commons Attribution 4.0 International license, see DOI: 10.25405/data.ncl.11208881.

REFERENCES

(1) Bui, M.; Adjiman, C. S.; Bardow, A.; Anthony, E. J.; Boston, A.; Brown, S.; Fennell, P. S.; Fuss, S.; Galindo, A.; Hackett, L. A.; Hallett, J. P.; Herzog, H. J.; Jackson, G.; Kemper, J.; Krevor, S.; Maitland, G. C.; Matuszewski, M.; Metcalfe, I. S.; Petit, C.; Puxty, G.; Reimer, J.; Reiner, D. M.; Rubin, E. S.; Scott, S. A.; Shah, N.; Smit, B.; Trusler, J. P. M.; Webley, P.; Wilcox, J.; MacDowell, N. Carbon Capture and Storage (CCS): The Way Forward. *Energy Environ. Sci.* **2018**, *11*, 1062–1176. https://doi.org/10.1039/C7EE02342A.

(2) D'Alessandro, D. M.; Smit, B.; Long, J. R. Carbon Dioxide Capture: Prospects for New Materials. *Angew. Chemie - Int. Ed.* **2010**, *49* (35), 6058–6082. https://doi.org/10.1002/anie.201000431.

(3) Pera-Titus, M. Porous Inorganic Membranes for CO_2 Capture: Present and Prospects. *Chem. Rev.* **2014**, *114* (2), 1413–1492. https://doi.org/10.1021/cr400237k.

(4) Mutch, G. A.; Qu, L.; Triantafyllou, G.; Xing, W.; Fontaine, M.-L.; Metcalfe, I. S. Supported Molten-Salt Membranes for Carbon Dioxide Permeation. *J. Mater. Chem. A* **2019**, *7*, 12951–12973. https://doi.org/10.1039/c9ta01979k.

(5) Cerón, M. R.; Lai, L. S.; Amiri, A.; Monte, M.; Katta, S.; Kelly, J. C.; Worsley, M. A.; Merrill, M. D.; Kim, S.; Campbell, P. G. Surpassing the Conventional Limitations of CO_2 Separation Membranes with Hydroxide/Ceramic Dual-Phase Membranes. *J. Memb. Sci.* **2018**, *567*, 191–198. https://doi.org/10.1016/j.memsci.2018.09.028.

(6) Tong, J.; Zhang, L.; Han, M.; Huang, K. Electrochemical Separation of CO_2 from a Simulated Flue Gas with High-Temperature Ceramic – Carbonate Membrane : New Observations. *J. Memb. Sci.* **2015**, *477*, 1–6. https://doi.org/10.1016/j.memsci.2014.12.017.

(7) Lu, B.; Lin, Y. S. Asymmetric Thin Samarium Doped Cerium Oxide-Carbonate Dual-Phase Membrane for Carbon Dioxide Separation. *Ind. Eng. Chem. Res.* **2014**, *53* (34), 13459–13466. https://doi.org/10.1021/ie502094j.

(8) Zuo, M.; Zhuang, S.; Tan, X.; Meng, B.; Yang, N.; Liu, S. Ionic Conducting Ceramic-Carbonate Dual Phase Hollow Fibre Membranes for High Temperature Carbon Dioxide Separation. *J. Memb. Sci.* **2014**, *458*, 58–65. https://doi.org/10.1016/j.memsci.2014.01.047.

(9) Xing, W.; Peters, T.; Fontaine, M. L.; Evans, A.; Henriksen, P. P.; Norby, T.; Bredesen, R. Steam-Promoted CO_2 Flux in Dual-Phase CO_2 Separation Membranes. *J. Memb. Sci.* **2015**, *482*, 115–119. https://doi.org/10.1016/j.memsci.2015.02.029.

(10) Rui, Z.; Anderson, M.; Li, Y.; Lin, Y. S. Ionic Conducting Ceramic and Carbonate Dual Phase Membranes for Carbon Dioxide Separation. *J. Memb. Sci.* **2012**, *417–418*, 174–182. https://doi.org/10.1016/j.memsci.2012.06.030.

(11) Zhang, L.; Xu, N.; Li, X.; Wang, S.; Huang, K.; Harris, W. H.; Chiu, W. K. S. High CO_2 Permeation Flux Enabled by Highly Interconnected Three-Dimensional Ionic Channels in

Selective CO_2 Separation Membranes. *Energy Environ. Sci.* **2012**, *5* (8), 8310–8317. https://doi.org/10.1039/c2ee22045h.

(12) Wade, J. L.; Lee, C.; West, A. C.; Lackner, K. S. Composite Electrolyte Membranes for High Temperature CO_2 Separation. *J. Memb. Sci.* **2011**, *369*, 20–29. https://doi.org/10.1016/j.memsci.2010.10.053.

(13) Chung, S. J.; Park, J. H.; Li, D.; Ida, J. I.; Kumakiri, I.; Lin, J. Y. S. Dual-Phase Metal-Carbonate Membrane for High-Temperature Carbon Dioxide Separation. *Ind. Eng. Chem. Res.* **2005**, *44* (21), 7999–8006. https://doi.org/10.1021/ie0503141.

(14) Lu, B.; Lin, Y. S. Synthesis and Characterization of Thin Ceramic-Carbonate Dual-Phase Membranes for Carbon Dioxide Separation. *J. Memb. Sci.* **2013**, *444*, 402–411. https://doi.org/10.1016/j.memsci.2013.05.046.

(15) Patrício, S. G.; Papaioannou, E. I.; Ray, B. M.; Metcalfe, I. S.; Marques, F. M. B. Composite CO_2 Separation Membranes : Insights on Kinetics and Stability. *J. Memb. Sci.* **2017**, *541* (July), 253–261. https://doi.org/10.1016/j.memsci.2017.07.008.

(16) Rui, Z.; Anderson, M.; Lin, Y. S.; Li, Y. Modeling and Analysis of Carbon Dioxide Permeation through Ceramic-Carbonate Dual-Phase Membranes. *J. Memb. Sci.* **2009**, *345*, 110–118. https://doi.org/10.1016/j.memsci.2009.08.034.

(17) Koenig, S. P.; Wang, L.; Pellegrino, J.; Bunch, J. S. Selective Molecular Sieving through Porous Graphene. *Nat. Nanotechnol.* **2012**, *7* (11), 728–732. https://doi.org/10.1038/nnano.2012.162.

(18) Monteleone, M.; Esposito, E.; Fuoco, A.; Lanč, M.; Pilnáček, K.; Friess, K.; Bezzu, C. G.; Carta, M.; McKeown, N. B.; Jansen, J. C. A Novel Time Lag Method for the Analysis of Mixed Gas Diffusion in Polymeric Membranes by On-Line Mass Spectrometry: Pressure Dependence of Transport Parameters. *Membranes (Basel).* **2018**, *8* (3), 1–15. https://doi.org/10.3390/membranes8030073.

(19) National Academies of Sciences, Engineering, and Medicine. *A Research Agenda for Transforming Separation Science*; The National Academies Press, 2019. https://doi.org/10.17226/25421.

For Table of Contents Only